Properties of water along the liquid-vapor coexistence curve via molecular dynamics simulations using the polarizable TIP4P-QDP-LJ water model

Brad A. Bauer and Sandeep Patel[a)]
Department of Chemistry and Biochemistry, University of Delaware, Newark, Delaware 19716, USA

(Received 19 May 2009; accepted 20 July 2009; published online 26 August 2009)

We present an extension of the TIP4P-QDP model, TIP4P-QDP-LJ, that is designed to couple changes in repulsive and dispersive nonbond interactions to changes in polarizability. Polarizability is intimately related to the dispersion component of classical force field models of interactions, and we explore the effect of incorporating this connection explicitly on properties along the liquid-vapor coexistence curve of pure water. Parametrized to reproduce condensed-phase liquid water properties at 298 K, the TIP4P-QDP-LJ model predicts density, enthalpy of vaporization, self-diffusion constant, and the dielectric constant at ambient conditions to about the same accuracy as TIP4P-QDP but shows remarkable improvement in reproducing the liquid-vapor coexistence curve. TIP4P-QDP-LJ predicts critical constants of T_c=623 K, ρ_c=0.351 g/cm^3, and P_c=250.9 atm, which are in good agreement with experimental values of T_c=647.1 K, ρ_c=0.322 g/cm^3, and P_c=218 atm, respectively. Applying a scaling factor correction (obtained by fitting the experimental vapor-liquid equilibrium data to the law of rectilinear diameters using a three-term Wegner expansion) the model predicts critical constants (T_c=631 K and ρ_c=0.308 g/cm^3). Dependence of enthalpy of vaporization, self-diffusion constant, surface tension, and dielectric constant on temperature are shown to reproduce experimental trends. We also explore the interfacial potential drop across the liquid-vapor interface for the temperatures studied. The interfacial potential demonstrates little temperature dependence at lower temperatures (300–450 K) and significantly enhanced (exponential) dependence at elevated temperatures. Terms arising from the decomposition of the interfacial potential into dipole and quadrupole contributions are shown to monotonically approach zero as the temperature approaches the critical temperature. Results of this study suggest that self-consistently treating the coupling of phase-dependent polarizability with dispersion interactions in classical water force fields may be an important effect for the extension of polarizable water force fields to reproduce properties along the liquid-vapor coexistence envelope as well as near critical conditions. More importantly, the present study demonstrates the rather remarkable transferability of a water model parametrized to a single state point to other thermodynamic states. Further studies are recommended. © *2009 American Institute of Physics*.
[DOI: 10.1063/1.3200869]

I. INTRODUCTION

One of the greatest strengths of molecular simulations, such as molecular dynamics (MD) or Monte Carlo, is the ability to probe state conditions that are difficult, expensive, or impossible to study experimentally. In order to achieve this, the molecular interaction models employed must necessarily be transferable to such conditions and/or environments; the *transferability* we discuss here is apart from that of transferability between similar chemical functionalities (series of linear alkanes, alcohols, etc.). Since aqueous environments are of fundamental importance to innumerable industrial and academic applications, interaction models of water continue to garner significant attention.[1–11]

Certainly, models can be successfully parametrized to reproduce target properties at various state points. Rather elegant work has been done to this effect by Chen and co-workers[12–17] leading to the fixed charge transferable potentials for phase equilibrium (TraPPE) force fields for fluid phase equilibria of a variety of polar and nonpolar species. Such force fields are able to reproduce the vapor-liquid coexistence curve and numerous properties of the bulk and vapor along the liquid-vapor binodal. One can reasonably ask about the possibility of constructing classical models (via fits to fluid properties at a single thermodynamic state point) that attempt to incorporate those physical effects that can allow for extension of such models to different state points *without* explicitly parametrizing to reproduce target properties under those conditions. Of course, such an undertaking assumes (1) that the physics incorporated is indeed responsible to some degree for the effects we are interested in capturing and (2) that the physics incorporated in the classical description of the model at a given state point is complete, and that the relevant components of the physics incorporated into the model contribute sufficiently at all thermodynamic state

[a)]Author to whom correspondence should be addressed. Electronic mail: sapatel@udel.edu.

TABLE I. Comparison of critical constants calculated for various water models and experiment. Method key is defined as follows: MD=molecular dynamics, MC=Monte Carlo, GEMC=Gibbs ensemble Monte Carlo, GD=Gibbs–Duhem, HS-GCMC=Hamilitonian scaling grand canonical Monte Carlo, Expt.=experiment, EC =long-range electrostatic treatment, VC=long-range van der Waals correction. Correction applied to the TIP4P-QDP-LJ data is taken as the multiplication factor required to achieve an agreement between the experimental critical property and the critical property estimated from the Wegner fit of experimental data listed in Ref. 53.

Model	T_c (K)	ρ_c (g/cm^3)	p_c (atm)	Method	Ref.
SPC	587	0.27	⋯	GEMC, EC	95
SPC/E	640	0.29	160	MD, EC, VC	96
SPC/E	630	0.308	⋯	MD, EC	45
GCPM	642.2	0.334	242	MC, EC, VC	20
Zhang	644.3	0.325	213	GEMC, VC	55
Exponential-6	645.9	0.297	183	HS-GCMC	54
TIP3P	578	0.272	124	GD, EC, VC	3
TIP4P	588	0.315	147	GEMC, VC	97
TIP4P/2005	640	0.31	144	GD, EC, VC	7
TIP4P/Ew	628	0.29	139	GD, EC, VC	7
TIP4P/ice	705	0.31	161	GD, EC, VC	7
TIP5P	521	0.337	85	GEMC, EC	98
TIP4P-FQ	574	0.33	227	MD, EC	18
TIP4P-FQ	543	0.352	⋯	MD, EC	Present work
TIP4P-QDP	557	0.355	93	MD, EC	Present work
TIP4P-QDP-LJ	623	0.351	250.9	MD, EC	Present work
TIP4P-QDP-LJ (correlation)	631	0.308	270.6	MD, EC	Present work
Expt. (Wegner Fit)	639.5	0.3674	⋯	Expt.	52 and 53
Expt.	647.1	0.322	218	Expt.	99

points. Although difficult to validate or discredit these assumptions, one can adopt a more "engineering" approach that would begin with a certain interaction model and add to it further physics. If the model performs well over extended ranges of thermodynamic state points (again, with the model parametrized at a single thermodynamic state point), one may place some degree of confidence in the transferability of the model and the relevance of the added physics in contributing to that transferability. In the current study, we take the approach to extend an existing model, the TIP4P-QDP water model of Bauer *et al.*,[8] and further refine the model by incorporating a coupling between the polarizability and nonbond interaction parameters [Lennard-Jones (LJ) constants]; the latter contains repulsion and dispersion contributions to the energy, the dispersion component rigorously tied to the atomic polarizability of interacting sites as an orientationally averaged instantaneous induced dipole-induced dipole interaction.

Recent efforts toward the development of nonadditive polarizable force fields have been a step forward in increasing the transferability of water force fields. Specifically, polarizable models allow for a simultaneous description of both liquid and gas phase electrostatics by allowing for the induction of higher dipoles in the condensed phase over that of a molecule in vacuum. Despite the ability of polarizable models to adopt charge configurations that can adequately reproduce simultaneously properties of a dense liquid environment and an isolated gas-phase environment (as well as intermediate densities), such water models often fail to reproduce the liquid-vapor coexistence curve and, as a result, underestimate critical constants (T_c, ρ_c). For example, the widely used TIP4P-FQ of Rick *et al.*[4] predicts critical temperature of $T_c=574$ K,[18] which is significantly lower than the experimental values of $T_c=647$ K. In general, for most water models, the liquid-vapor coexistence curve drastically underestimates the density of the liquid phase with increasing temperature, suggesting weak cohesive forces above ambient temperatures; the simple point charge/extended (SPC/E) water model is a particularly good force field for representing the vapor-liquid coexistence of water.[19] A more recent water model based on a recent Gaussian charge polarizable model (GCPM) is one of the few water models that when parametrized to a single thermodynamic state point has been able to fairly accurately represent bulk liquid properties along the binodal without further parameterization.[20] We note that although the structure and condensed phase liquid energetics for the GCPM model[20] were fit to ambient conditions, the model was fit to reproduce vapor-liquid equilibrium (VLE) coexistence properties (using Gibbs ensemble Monte Carlo simulations). Thus, the GCPM model reproduces quite well the vapor-liquid coexistence curve (Fig. 3, top panel in Ref 20) since those data were incorporated into the fitting procedure; VLE properties in this sense are not truly predictive at least in the case of pure water. The most accurate condensed-phase classical pure water force field is the TIP4P-2005 4-site model of Abascal and co-worker.[7] Parametrized to reproduce the temperature of maximum density of pure water, the TIP4P-2005 model predicts the phase diagram of water from solid to vapor remarkably well. The model predicts a critical temperature of 640 K, only 7 K below the experimental value. The critical parameters of the model are given in Table I and the VLE curve is shown as an

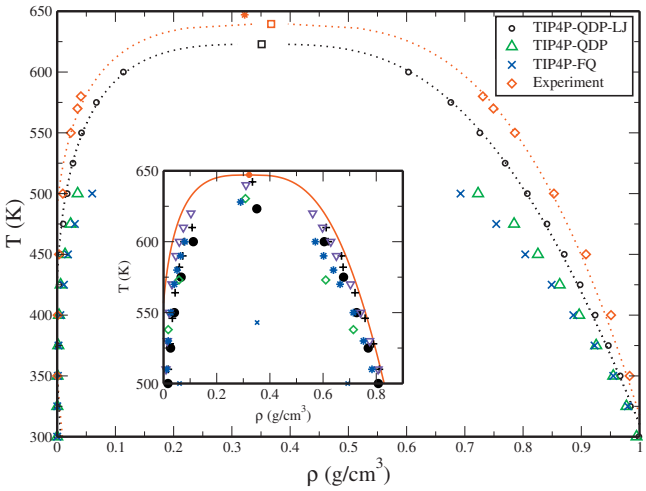

FIG. 1. Liquid-vapor coexistence curves. The dotted lines are the functional fit using the Wegner expansion [Eq. (15)] and the squares represent the calculated critical point for the given set. For the experimental data, the Wegner expansion results in an underestimation of the experimental critical point (star). TIP4P-QDP-LJ is shown to improve the reproduction of the coexistence curve over TIP4P-FQ and TIP4P-QDP. The inset compares the liquid-vapor coexistence curve as predicted by TIP4P-QDP-LJ (circles), GCPM (+) (Ref. 20), SPC/E (diamonds) (Ref. 45), TIP4P-2005 (triangles) (Ref. 7), TIP4P-EW (stars) (Ref. 7), and TIP4P-FQ (x) water models and experiment (solid line).

inset to Fig. 1 (also shown are the results from other existing water models).

That both the SPC/E and GCPM water models incorporate condensed phase polarization effects (either in a mean-field manner as in the former case or explicitly as in the latter) suggests the importance of water polarizability for reproducing bulk and vapor properties over broad ranges of thermodynamic state points. Furthermore, it is well known that an isolated water molecule has a polarizability of ~ 1.47 Å^3.[21] However, like many other polarizable models, TIP4P-FQ features a polarizability (1.1 Å^3) well below this gas-phase value in order to achieve stable dynamics and reproduce condensed phase properties at 298 K. Although recent *ab initio* studies support a reduced molecular polarizability in the condensed phase,[22–24] the parametrization of a static polarizability inherently restricts enhancement of polarizability (and consequently molecular cohesion) in less dense environments,[22] such as those observed at higher temperatures and particularly in the interfacial regions at elevated temperatures. Such arguments are the basis for the TIP4P-QDP model,[8] which modulates molecular polarizability in response to its local environment by coupling molecular polarizability (via atomic hardness) to atomic charge. The focus of this work is to incorporate polarizability dependence in the repulsion and dispersion terms via incorporation of a charge dependence in the LJ terms. The resulting model, TIP4P-QDP-LJ, will be parametrized to reproduce properties at 298 K, ideally behaving similarly to the TIP4P-QDP model from which it is derived. In order to assess the transferability of this model, we examine its ability to reproduce the liquid-vapor coexistence curve (compared to TIP4P-QDP and other state-of-the-art models) as well as its ability to predict critical constants and various bulk liquid and vapor phase properties at higher temperatures including dielectric and self-diffusion constants, enthalpy of vaporization, and surface tension. We intend to demonstrate that incorporation of phase-dependent polarizability, coupled with a charge dependence of the repulsion-dispersion interactions, within a classical polarizable force field allows for a systematically improved representation of the liquid-vapor coexistence properties of liquid water as well as predicting the pure water critical temperature and density to within 2.5% and 4.3% error, respectively. Our results also suggest an alternative approach to transferable force fields for phase-equilibrium calculations (and indeed for water models appropriate for use in modeling of solvated biomacromolecular and ionic systems in general) based on parametrization to single state points; this approach obviates the need for knowing *a priori* the coexistence behavior of a system to which a force field can be parametrized. In addition to characterizing the TIP4P-QDP-LJ on the basis of its ability to reproduce properties along the coexistence curve relative to well-established experimental trends, we exercise the predictive nature of the model to calculating hydrogen bonding data and interfacial potentials at these state points.

II. FORCE FIELDS AND COMPUTATIONAL METHODS

A. Charge equilibration force fields

The charge equilibration (CHEQ) formalism offers one convenient route for incorporating local chemical environmental dependence of the molecular polarizability. This formalism is based on Sanderson's[25] idea of electronegativity equalization, which states that the polarization of the electronic density (modeled as a distribution of partial charges in a classical representation) is affected by the redistribution of charge density within the molecule in order to equalize the instantaneous electrostatic chemical potential in the presence of external electric fields arising from the surrounding molecules. The directionality and ease of charge redistribution are determined by physical properties of individual atoms. The reader is referred to the literature for additional information on CHEQ methods.[4,25–35]

The CHEQ electrostatic energy of an N-atom molecule in the absence of an external electric field, each atom carrying partial charge Q_i, is

$$E(Q) = \sum_{i=1}^{N} \left(\chi_i Q_i + \frac{1}{2} \eta_i Q_i^2 \right) + \sum_{i<j}^{N} Q_i Q_j J_{ij} + \lambda \left(\sum_{i=1}^{N} Q_i - Q_{\text{tot}} \right), \quad (1)$$

where χ_i are atom electronegativities and η_i are atomic hardnesses. The J_{ij} terms represent the interatomic hardness terms for each pair of atoms i and j within a molecule. A standard Coulomb interaction is employed between each pair of atoms located on different molecules. The last term in Eq. (1) describes a molecular charge constraint applied to the entire molecule and enforced via the Lagrange multiplier λ.

B. Phase-dependent polarizable model

While polarizable water force fields in general incorporate further physics in classical force fields relative to their nonpolarizable analogs, these force fields are just now beginning to consider the *variation* in molecular polarizability with phase. Recent studies have demonstrated the difference in molecular polarizability for molecules in the gas phase compared to those in a condensed-phase environment.[22–24] The TIP4P-QDP model of Bauer *et al.*[8] offers a means to introduce phase-dependent polarizability of water into a classical simulation. The model explicitly modifies the electrostatic energy expression of the CHEQ formalism such that the η and χ parameters are functions of the M-site charge (which carries the charge for the oxygen atom),

$$E(Q) = \sum_{i=1}^{N} \chi_i(Q_M)Q_i + \frac{1}{2}\sum_{i=1}^{N} \eta_i(Q_M)Q_i^2 + \sum_{i<j}^{N} J_{ij}(Q_M)Q_iQ_j + \lambda\left(\sum_{i=1}^{N} Q_i - Q_{\text{tot}}\right). \tag{2}$$

The Q_M-dependence of each term is invoked via a scaling function $g(Q_M)$ that monotonically modulates the hardnesses (affecting the molecular polarizability) and electronegativities (affecting the molecular dipole moment) from the parametrized gas phase value to an appropriate condensed phase value,

$$\boldsymbol{\eta}(Q_M) = g(Q_M)\cdot\boldsymbol{\eta}, \tag{3}$$

$$\boldsymbol{\chi}(Q_M) = \frac{g(Q_M)}{h(Q_M)}\boldsymbol{\chi} = [1 + p(g(Q_M) - 1)]\cdot\boldsymbol{\chi}, \tag{4}$$

where p is an empirical parameter that controls the magnitude of scaling of χ relative to that of η in order to afford better control the dielectric constant and average bulk dipole moment. TIP4P-QDP couples the well-established trend of increasing dipole moment (simplified as the magnitude of charge on the oxygen site) upon condensation to an increased scaling $(g(Q_M)>1)$ in the hardness matrix, mimicking phase-dependent effects on polarizability. The result is a polarizability distribution in the condensed phase (centered about $\alpha=1.31$ Å^3), which offers a 6.5% reduction in the parametrized gas phase value in good agreement with *ab initio* estimates.[24] We estimate molecular polarizability for TIP4P-QDP water via the expression[8]

$$\alpha_{\beta\gamma}(Q_M) \approx \frac{\alpha_{\beta\gamma}}{\xi(Q_M)} - \left(\frac{\nabla_M g(Q_M)\langle R_\beta|\mathbf{J}^{-1}(\mathbf{r})|\hat{\mathbf{M}}\rangle}{|g(Q_M)|^2 h(Q_M)}\right) \times\left[p\chi_M\langle R_\beta|\mathbf{J}^{-1}(r)|\hat{\mathbf{M}}\rangle + \frac{1}{2}\mu_\gamma\right], \tag{5}$$

which provides a leading-order approximation of the polarizability in the absence of a fully nonlinear treatment. In the above expression, $\alpha_{\beta\gamma}$ is the $\beta\gamma$-element of the gas-phase molecular polarizability tensor, $\nabla_M g(Q_M)$ is the derivative of the scaling function with respect to Q_M, $\mathbf{R}_\beta$ is the β-position vector, $\hat{\mathbf{M}}$ is a matrix that selects elements associated with the M-site (since we have chosen our hardness elements to only depend on the oxygen charge), and μ_γ is the γ-component of the dipole moment. We see the charge-dependent polarizability differs from the unscaled (gas-phase) value by a multiplicative factor $\xi(Q_M) = g(Q_M)h(Q_M)$ and additive terms, which are related to the M-site hardness and dipole moment, respectively. These additive terms of equal magnitude and opposite sign are small compared to the first term and do not greatly influence $\alpha(Q_M)$. We direct interested readers to Ref. 8 for a more detailed discussion of the TIP4P-QDP model.

C. TIP4P-QDP-LJ

TIP4P-QDP-LJ builds upon the TIP4P-QDP model by modification of the LJ interaction potential. The standard LJ potential defines the interaction between two sites, i and j, as

$$E(r_{ij}) = 4\epsilon_{ij}\left[\left(\frac{\sigma_{ij}}{r_{ij}}\right)^{12} - \left(\frac{\sigma_{ij}}{r_{ij}}\right)^{6}\right], \tag{6}$$

where r_{ij} is the distance between the two LJ sites. Here ϵ and σ correspond to the well-depth and LJ radius, respectively, but are treated as empirical parameters. The r^{-12} term describes the repulsive interaction between two sites while the r^{-6} term represents the attractive or dispersive interactions. Equivalently, the LJ potential implemented in CHARMM[36,37] is

$$E(r_{ij}) = \epsilon\left[\left(\frac{R_{\min,ij}}{r_{ij}}\right)^{12} - 2\left(\frac{R_{\min,ij}}{r_{ij}}\right)^{6}\right], \tag{7}$$

where $R_{\min,ij}$ is the radius at which the interaction potential between sites i and j is a minimum and $R_{\min,ij}=2^{1/6}\sigma_{ij}$. We remark that Eqs. (6) and (7) can be generalized by combining the empirical parameters into collective repulsive and dispersive constants,

$$E(r_{ij}) = \frac{A}{r_{ij}^{12}} - \frac{C}{r_{ij}^{6}}. \tag{8}$$

Despite the empirical treatment of the r^{-6} term, it is related to the sum of contributions arising from dipole-dipole, dipole-induced dipole, and dispersion interactions,[38]

$$V(r) = -\frac{2}{3}\frac{\mu_i^2\mu_j^2}{k_BTr_{ij}^6} - \frac{(\mu_i^2\alpha_j + \mu_j^2\alpha_i)}{r_{ij}^6} - \frac{3I_iI_j}{2(I_i+I_j)}\frac{\alpha_i\alpha_j}{r_{ij}^6}, \tag{9}$$

where μ_i, α_i, and I_i are the dipole moment, the polarizability, and the ionization potential of the ith species, *respectively*.

It is established that polarizability modulation in TIP4P-QDP model is coupled to the charge of the M-site, Q_M. Therefore, coupling the LJ parameters to charge will allow us to couple changes in the effective size of TIP4P-QDP molecules with changes in polarizability. We expand the repulsive and dispersive constants quadratically with respect to charge as has been done previously by Chen *et al.*,[9]

$$A = A_0 + A_1\times Q_{\text{av},ij} + A_2\times Q_{\text{av},ij}^2,$$
$$C = C_0 + C_1\times Q_{\text{av},ij} + C_2\times Q_{\text{av},ij}^2. \tag{10}$$

We note that each water molecule has a single LJ site centered on the oxygen atom. However, the oxygen's charge is

TABLE II. Nonbond parameters for TIP4P-QDP and TIP4P-QDP-LJ.

Parameter	TIP4P-QDP-LJ	TIP4P-QDP
A_0 (kcal mol^{-1} Å^{-12})	1 116 209	1 170 544
A_2 (kcal mol^{-1} Å^{-12} esu^{-2})	55 810	0
C_0 (kcal mol^{-1} Å^{-6})	1419.5	1165
C_2 (kcal mol^{-1} Å^{-6} esu^{-2})	−141.95	0

carried by the M-site of the molecule. Also following the convention of Chen *et al.*, we base the charge dependence on the average M-site charge between molecules i and j,

$$Q_{\mathrm{av},ij} = \frac{Q_{M,i} + Q_{M,j}}{2}. \tag{11}$$

In an effort to simplify the parametrization process, A_1 and C_1 were set to zero, leaving four adjustable parameters. We will now briefly discuss the selection of the remaining parameters. Since the model developed should behave similarly to TIP4P-QDP at 298 K and 1 atm, we parametrized to only this state point. Specifically, the condensed-phase density, enthalpy of vaporization, gas-phase dimer distance, and dimerization energy were considered. Using the original LJ parameters of TIP4P-QDP and the average M-site charge for a TIP4P-QDP dimer, we determined the appropriate values for the constants in the charge dependent term as

$$A_0 = \frac{A}{1.0 + x_A Q^2_{\mathrm{av,dimer}}},$$
$$C_0 = \frac{C}{1.0 + x_C Q^2_{\mathrm{av,dimer}}}. \tag{12}$$

Such an approach allows the specification of extent of the influence charge has on the LJ parameters, since $A_2 = xA_0$ and $C_2 = xC_0$. The sign designated to each of the second-order coefficients dictates the behavior upon entering condensed-phase environments. Since water polarizability is lower in bulk than in the gas phase, the increase in Q^2_{av} associated with transition into the condensed phase is coupled with an increase in the repulsive constant[9] and a decrease in the dispersion constant. That is, A_2 is positive and C_2 is negative. We remark that this convention results in a negative value of x_C as described above. Furthermore, the LJ parameter C was scaled (by ~10%) to account for the decrease in this term upon condensation. The LJ parameters used in this work are presented in Table II. The electrostatic parameters have not been adjusted from the previously reported TIP4P-QDP model. The model, therefore, features a gas phase polarizability of $\alpha_{\mathrm{isotropic}} = 1.4$ Å^3 and a gas-phase dipole moment of $\mu_{\mathrm{gas}} = 1.85$ D. Additionally, TIP4P-QDP-LJ features gas-phase dimer properties ($R_{\mathrm{OO}} = 2.90$ Å and $E_{\mathrm{dimer}} = -4.85$ kcal/mol) similar to those of TIP4P-QDP, $R_{\mathrm{OO}} = 2.91$ Å and $E_{\mathrm{dimer}} = -4.67$ kcal/mol. Finally, we remark that the weight of charge dependence on the LJ terms is rather modest at 5% on the repulsive constant and 10% on the attractive term, in line with the reduction in polarizability of TIP4P-QDP in the condensed phase.

D. Simulation details

MD simulations were performed using CHARMM.[36,37] For the parametrization and characterization of the model, constant *NPT* simulations were conducted in a bulk system of 216 water molecules. Conditionally convergent long-range interactions were treated using particle mesh Ewald[39] with $\kappa = 0.37$ and 20 grid points in each direction (fast Fourier transform (FFT) grid spacing). Fictitious charge degrees of freedom are assigned masses of 0.000 069 kcal/(mol ps^2). The Nose-Hoover[40] method was implemented to couple the charge degrees of freedom to a thermostat at 1 K; the thermostat was assigned a mass of 0.005 kcal/(mol ps^2). A 0.5 fs time step was implemented for propagating the classical equations of motion using Verlet leapfrog integrator.

Interfacial simulations of the liquid-vapor interface were conducted at constant *NVT* and over the range of 300–600 K (every 25 K). Simulations of TIP4P-QDP-LJ and TIP4P-FQ employed a slab of 3235 water molecules in box with dimension $32 \times 32 \times 224$ Å^3. TIP4P-QDP interfacial simulations were conducted using a smaller system of 1024 molecules in a $24 \times 24 \times 100$ Å^3 simulation cell. Periodic boundary conditions were considered in each dimension. For these simulations, the number of grid points was increased to 30 in each the x and y directions (transverse direction) and 128 in the z-direction (longitudinal direction); κ was modified to 0.33. Other simulation protocol followed that of the bulk simulations. Interfacial simulation results are based on at least 4 ns of equilibrated data for each temperature.

Condensed phase properties at elevated temperatures ($T > 325$ K) were performed at constant *NVT*. Here, 216 water molecules were simulated in a cubic box with dimensions selected to reproduce the equilibrium condensed phase density determined from the interfacial simulations at each temperature. Condensed-phase data are based on ~10 ns of sampling. All other simulation details are the same as those listed above for the condensed-phase simulations at $T = 298$ K. Additionally, simulations were conducted at the experimental coexistence densities, which deviate nontrivially from the simulation densities at near-critical temperatures. Finally, all simulations implemented a harmonic wall potential to eliminate divergences in charge at increased temperatures.[18] This potential was applied to each atom with a force constant of 200.0 kcal mol^{-1} esu^{-2}. Furthermore, the charges at which the potential was turned on were selected such that they were significantly outside the range of those normally experienced in simulation; that is, the potential was invoked outside the range of $-1.6 < Q_M < -0.6$ for the M-site and outside $0.3 < Q_{\mathrm{H}} < 1.2$ for the hydrogen atoms.

III. RESULTS

In this section we present the results from bulk simulations and simulations of the liquid-vapor interface using the TIP4P-QDP-LJ model at $T = 300-600$ K. Particular emphasis is placed on the similarity in the properties of TIP4P-QDP-LJ and TIP4P-QDP models at $T = 298$ K (Table III), as this is the temperature at which both models were parametrized (with focus on reproducing the liquid density and

TABLE III. Comparison of dimerization energies and condensed-phase properties calculated at 298 K and 1 atm for various water models and experiment.

Model	$-E_{dimer}$ (kcal/mol)[a]	ρ_{liq} (g/cm^3)	ΔH_{vap} (kcal/mol)	D_s ($\times 10^{-9}$ m^2/s)	ϵ
TIP3P[b]	6.50	1.002	10.41	5.1	88(±6)
TIP4P[b]	6.24	1.001	10.65	3.22	50
TIP4P/2005[c]	7.12	0.9979	10.89	2.08	60
TIP4P/EW[d]	6.81	0.9954	10.583	2.4(±0.06)	63.9(±0.9)
TIP5P[b]	6.79	0.999	10.46	2.6	82±2
TIP4P-FQ[e]	4.50	1.000	10.49	1.9(±0.1)	79(±8)
TIP4P-QDP[f]	4.67	0.9954	10.55	2.46(±0.04)	85(±1)
TIP4P-QDP-LJ	4.85	0.998	10.47(±0.01)	2.30(±0.04)	77(±11)
Expt.[g]	5.44(±0.7)	0.997	10.51	2.30	78

[a]Dimerization energies for TIP3P and TIP4P are taken from Ref 6; those for TIP4P/2005, TIP4P/EW, and TIP5P are taken from Ref 94. All other values are from the same reference as other properties.
[b]Reference 1, and references therein.
[c]Reference 89.
[d]Reference 59.
[e]Reference 4.
[f]Reference 8.
[g]References 63 and 90–92. Mas *et al.* (Ref. 93) suggested an empirical estimate of the dimerization energy for water of 5.00±0.7 kcal/mol based on corrections to the zero point energy.

enthalpy of vaporization). Although the goal of this work is to explore the ability of the TIP4P-QDP-LJ model to reproduce the liquid-vapor coexistence curve by incorporating additional physics consistent with modulation of polarizability in different environments (and parametrization of the model at a single thermodynamic state point), we did not target properties at elevated temperatures when parametrizing the TIP4P-QDP-LJ model. We believe such an approach is most satisfying for demonstration of the benefits of a fully phase-dependent polarizable model (i.e., modulation of atomic hardness and dispersion interactions). Table III shows the properties for several three-site and four-site water models including the current work. In general, the current water model reproduces a wide range of bulk liquid water properties at 298 K (as parametrized) and compares favorably with existing models. Although liquid density is robustly reproduced by most water models, more variation is apparent in properties such as gas-phase dimer energy, vaporization enthalpy, diffusion constant, and dielectric constants. We note that in terms of transferability, the polarizable models are able to capture the gas-phase dimer energy (and structure) as well as a broad range of condensed phase properties. We note that the nonpolarizable models such as TIP3P, TIP4P, and TIP4P-2005 overestimate the favorability of the gas-phase dimer (Table III). This enhancement of dimer interactions most likely accommodates a more cohesive vapor phase at elevated temperatures and in part assists in the more accurate reproduction of the vapor envelope of the two-phase binodal by the TIP4P-2005 water model.[67,89]

A. Density profiles and liquid-vapor coexistence

We consider the density profiles for TIP4P-QDP-LJ as a function of the z-position at various temperatures in Fig. 2(a). As anticipated, increases in temperature result in decreasing densities in the liquid phase and corresponding increase in the density of the vapor phase. At $T=600$ K (our highest temperature simulated), there still exist two distinct equilibrium phases, indicating that this temperature is in the subcritical region. To quantify these results, density profiles computed at each simulated temperature were fit to an error function of the form[41–43]

$$\rho(z) = \frac{1}{2}(\rho_L + \rho_V) - \frac{1}{2}(\rho_L - \rho_V)\mathrm{erf}\left(\frac{z - z_0}{\delta_e}\right), \tag{13}$$

where ρ_L and ρ_V are the densities of the liquid and vapor phases, respectively, δ_e is an intrinsic interfacial thickness, and z_0 is the position of the Gibbs dividing surface. We acknowledge that density profiles are also commonly fit to a hyperbolic tangent function of the form[44–48]

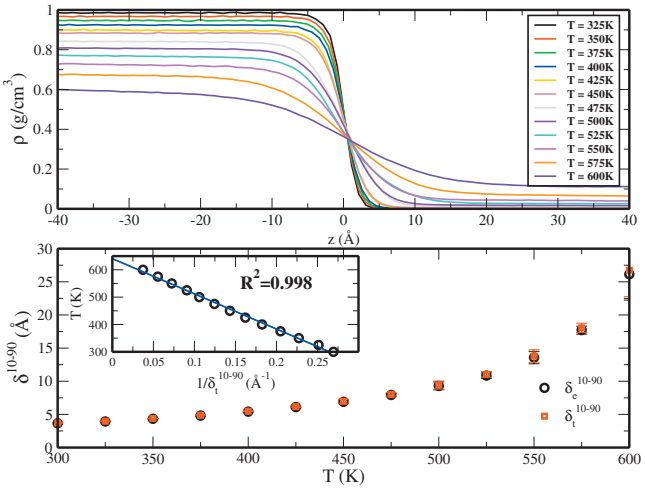

FIG. 2. Density profiles as a function of z-position (relative to the Gibbs dividing surface) at various temperatures (upper panel) and the temperature dependence of interfacial width (lower panel). The inset of the lower panel demonstrates a strong linear relation ($R^2=0.998$) for temperature vs the reciprocal of the interfacial width. The solid blue line in this inset is the linear fit to the hyperbolic tangent data and is expressed as $T=640.7(\pm 3.7)-1286(\pm 22)/\delta_t^{10-90}$.

TABLE IV. Results of error function and hyperbolic tangent function fits to the density profiles at 300 K $\leq T \leq$ 600 K. Interfacial thicknesses are expressed using the 10-90 criteria and are obtained from the inherent interfacial thicknesses via the following relationships: $\delta_e^{10-90}=1.8124\delta_e$ and $\delta_t^{10-90}=2.1972\delta_t$.

	Error function fit			Hyperbolic tangent fit		
T (K)	ρ_{liq} (g/cm^3)	ρ_{vap} (g/cm^3)	δ_e (Å)	ρ_{liq} (g/cm^3)	ρ_{vap} (g/cm^3)	δ_t (Å)
300	0.9989(4)	0.0000(1)	3.66(10)	0.9992(4)	0.0000	3.71(10)
325	0.9843(4)	0.0001(1)	3.93(3)	0.9846(4)	0.0000	3.98(3)
350	0.9667(2)	0.0002(1)	4.34(4)	0.9671(2)	0.0000	4.40(4)
375	0.9465(4)	0.0007(1)	4.82(9)	0.9468(5)	0.0003(1)	4.88(9)
400	0.9237(2)	0.0017(2)	5.41(7)	0.9241(2)	0.0014(2)	5.47(7)
425	0.8980(5)	0.0034(3)	6.10(12)	0.8984(5)	0.0030(3)	6.17(12)
450	0.8707(5)	0.0060(3)	6.90(30)	0.8712(5)	0.0056(4)	6.98(30)
475	0.8410(7)	0.0105(5)	7.93(24)	0.8415(7)	0.0100(5)	8.03(25)
500	0.8073(9)	0.0173(5)	9.30(58)	0.8078(9)	0.0167(5)	9.43(59)
525	0.7692(7)	0.0271(13)	10.9(4)	0.7699(7)	0.0265(13)	11.0(4)
550	0.7258(17)	0.0418(9)	13.6(9)	0.7265(17)	0.0410(9)	13.8(10)
575	0.6760(24)	0.0674(15)	17.7(7)	0.6769(24)	0.0663(14)	18.1(7)
600	0.6032(72)	0.1137(48)	26.1(39)	0.6043(73)	0.1120(47)	26.8(40)

$$\rho(z) = \frac{1}{2}(\rho_L + \rho_V) - \frac{1}{2}(\rho_L - \rho_V)\tanh\left(\frac{z - z_0}{\delta_t}\right), \tag{14}$$

where δ_t is the intrinsic interfacial thickness associated with the hyperbolic tangent fit. The results of these fits are presented in Table IV. Both the error function fit and hyperbolic tangent fit show results in similar condensed phase densities. Although ρ_{liq} from the hyperbolic tangent fit are consistently higher than those from the error function fit, the values between both functional fits generally agree within the uncertainty associated with these values. Comparison of the vapor densities between the two fits shows a similar result, although the ρ_{vap} from the error function fit are consistently higher. We also present the interfacial thicknesses obtained from each fit in Table IV. The differences in curvature of the two functional forms result in intrinsic thicknesses that are significantly different. Direct comparison of the thicknesses obtained from each fit is possible through the conversion of the intrinsic thicknesses to those using the "10-90" definition. This describes the width over which the density changes from 10% to 90% of the bulk density value, and it is easily obtained via the relationships $\delta_e^{10-90}=1.8124\delta_e$ and $\delta_t^{10-90}=2.1972\delta_t$. The interfacial thicknesses are plotted against temperature in Fig. 2(b) and are shown to increase exponentially. This behavior follows the trends observed in the density profiles; as the system reaches the critical point, there will be no distinction between liquid and vapor phases or equivalently there will be infinite interfacial thickness at the critical point (we acknowledge that in the present study, we forego an analysis of the fluctuations in density in liquid and vapor phases in the near-critical region). To further examine this, we plotted the temperature as a function of the reciprocal of interfacial thickness in the inset of Fig. 2(b). Linear regression analysis shows a strong correlation between these data ($R^2=0.998$). Intriguingly, the y-intercept is ~640 K, which is close to the various values we compute for the critical temperature (to be discussed at length below) as well as the experimental critical temperature of water (647 K). Upon closer examination, we observe what appears to be the onset of a greater curvature for smaller values of the 10-90 thickness. This suggests a higher predicted value for the critical temperature, which would only approach more closely the experimental value compared to the purely linear fit. This suggests that such an approach can yield a reasonable estimate of the critical temperature of the model via MD simulations, although more extensive tests across spanning a much broader set of liquids must be inevitably performed to arrive at a definitive conclusion. It is remarkable that such a simple analysis yields a value comparable to the experimental measurement.

The average density for the liquid and vapor phases at each temperature was then used to generate the liquid-vapor coexistence curve (Fig. 1). From the liquid-vapor coexistence curve, the critical temperature and density can be estimated using the law of rectilinear diameters and a three-term Wegner expansion of the form[49–51]

$$\rho_{LV} = \rho_c + C_2\left(1 - \frac{T}{T_c}\right) \pm \left\{B_0\left(1 - \frac{T}{T_c}\right)^{\beta} + B_1\left(1 - \frac{T}{T_c}\right)^{\beta+\Delta}\right\}. \tag{15}$$

Here, ρ_c is the critical density, T_c is the critical temperature, and B_0, B_1, and C_2 are variable constants. These parameters were simultaneously fit using a simulated annealing protocol. During this fit, the constants β and Δ were set equal to their standard values as established from renormalization group theory: $\beta=0.325$ and $\Delta=0.50$.[49] Using this protocol, the critical constants for TIP4P-QDP-LJ were determined to be $T_c=622.87$ K, $\rho_c=0.3511$ g/cm^3 for the error function data and $T_c=623.21$ K, $\rho_c=0.3508$ g/cm^3 for the hyperbolic tangent fit. In order to assess the uncertainty associated with this approach, the critical constants were also determined by fitting Eq. (15) to available experimental data.[52,53] This exercise results in an underprediction of the experimental critical temperature by 7.6 K and overprediction of the critical density of water by 0.045 g/cm^3, differences of 1.2% and 14%, respectively. In light of this variation associated with the

fitting procedure, we investigate the effect of scaling our predicted critical constants by factors determined from the differences in the actual experimental and fitted experimental data to obtain "corrected" estimates of 631 K and 0.308 g/cm^3 for TIP4P-QDP-LJ. These values are comparable to experiment and demonstrate a degree of accuracy commensurate with values predicted by several other models (Table I); we emphasize that the corrected values employ an *ad hoc* scaling that is not in general applicable, particularly in situations where no experimental data are known *a priori*. We reiterate that the scaling factor arises from the exercise of fitting the experimental water VLE data to the renormalization theory and we do not assert the use of such scaling factors in a general sense. From the data of Table I, it is evident that the current results for critical temperature and density are not the most accurate relative to experiment; force fields such as those of Errington and Panagiatopouls[54] and the GCPM model of Paricaud *et al.*[20] predict more accurate critical parameters. However, it is important to keep in mind that the force fields used in these studies were constructed by fitting to the VLE curve. This is a nontrivial distinction when assessing the results of this study to previous work. The comparison between TIP4P-QDP-LJ, TIP4P-FQ, and TIP4P-QDP results is most relevant since these models are closely related in that they are polarizable and share similar condensed phase properties. The coexistence curves for TIP4P-FQ and TIP4P-QDP underestimate the condensed phase density at high temperatures, with TIP4P-QDP demonstrating somewhat better agreement with experiment. This is anticipated on the basis of the generally higher polarizability of the TIP4P-QDP model and its enhancement at higher temperatures (rarefied densities approaching vaporlike environments in which water polarizability asymptotes to the isolated-molecule value of 1.4 $Å^3$ as represented in the TIP4P-QDP models). Notably, the increased explicit electronic polarizability included via the dynamical charges and environment-dependent polarizability appears to marginally affect the coexistence curve. However, we observe that the effects of polarizability (static and dynamic) as incorporated in the dispersion contributions [Eq. (9)] appear to have a substantial effect in modulating the cohesiveness of the liquid phase. In this respect, the TIP4P-QDP-LJ model demonstrates the added importance of including the variation in LJ parameters; this effect is directly related to the variation in molecular polarizability in different environments. Finally, we note that the predicted coexistence curve is nontrivially dependent on the simulation protocol. The difference in the critical constants calculated for TIP4P-FQ in this work and in Ref. 18 illustrates such dependence. Yoshii *et al.*[18] predict a critical temperature of 574 K, which is ~5% lower than the value predicted here; their critical density of 0.33 g/cm^3 is ~7% lower than the value calculated in this work; however, we note that that study was based on *NVT* simulations of a slightly modified form of TIP4P-FQ mapping out a $P\rho T$ surface to which the authors fit an equation of state. Since the protocols used in the two studies are different, we note that some care must be taken with the interpretation of the models. Admittedly, the use of a long-range correction for dispersion (LJ) interactions (neglected in the current study) may improve the agreement of the simulated coexistence curves and experiment. Such a term is likely to increase the cohesion within the bulk and shift the coexistence points closer to experiment.

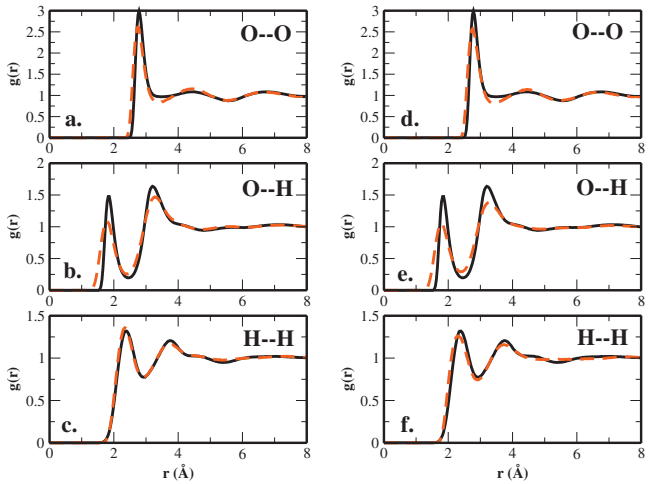

FIG. 3. RDFs for TIP4P-QDP-LJ at 298 K. Panels (a)–(c) compare the TIP4P-QDP-LJ O–O, O–H, and H–H radial distributions with combined neutron and x-ray diffraction data from Soper (Ref. 56) using the "HASYlab" set. Panels (d)–(f) are the analogous RDFs as (a)–(c) except using the "HASYlab new" experimental set (Ref. 56).

Recent studies such as those of Zhang *et al.*[55] perform extremely well in reproducing the coexistence properties of a flexible water model; the authors also show excellent agreement of their water model to experimental virial coefficients. We comment here that despite these strengths of the water model, the authors do not show data on other properties in order to more rigorously assess the water model across a wider range of properties. We believe that such approaches more rigorously define the quality of any given water model.

B. Radial distribution functions

Radial distribution functions (RDFs) for TIP4P-QDP-LJ at 298 K along with experimentally determined results are shown in Fig. 3; results for oxygen-oxygen, oxygen-hydrogen, and hydrogen-hydrogen RDFs are shown. Experimental measurements include results from recent joint structural refinement using both x-ray and neutron diffraction measurements [HASYlab (new)] in conjunction with the empirical potential structure refinement (EPSR) method.[56]

The TIP4P-QDP-LJ model appears to capture the position of the first peak as determined by the combined (x-ray and neutron) structural refinement measurements as well as the old and new neutron diffraction measurements; variance between the different experimentally determined first peak positions ranges from 0 to 0.4 Å. This is also consistent with EPSR refinement of the diffraction data.[56] The first peak height of the oxygen-oxygen RDF is overestimated relative to all experimental data as well as EPSR simulation-based estimates (the latter is demonstrated in Fig. 3); this is also observed for most water models including the recent TIP4P-2005 water model. The minimum following the first peak for the TIP4P-QDP-LJ model is not as well defined compared to experiment and other water models such as the TIP4P-2005.

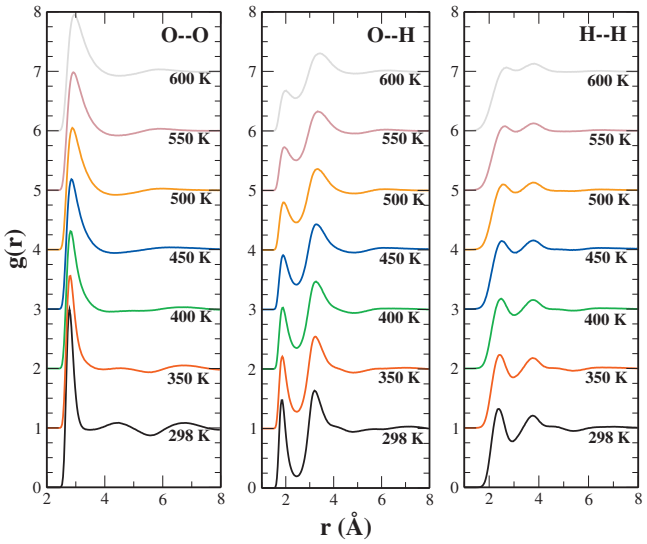

FIG. 4. TIP4P-QDP-LJ RDFs for O–O (left panel), O–H (center panel), and H–H (right panel) interactions. The RDFs for simulations at temperatures of 298–600 K are shown to demonstrate the loss of structure at elevated temperatures.

However, the shape of the oxygen-oxygen RDF predicted by the current water model is consistent with the TIP4P family of water models originally parametrized.[4,6,8]

The TIP4P-QDP-LJ oxygen-hydrogen RDFs show slightly longer first peak positions relative to the combined x-ray neutron diffraction based EPSR results; furthermore, the first peak heights are consistently higher and the first minima shallower. For the hydrogen-hydrogen RDFs, the current model fares the best in terms of matching experimental peak positions and peak heights.

Finally, we note that for the oxygen-oxygen and oxygen-hydrogen RDFs, the force field based distribution functions exhibit a steeper leading edge toward the first peak; this has been attributed to the hard, short-range repulsion implicated with the LJ 12-6 potential[56] (also used in this study). It appears that modulation of this form using varying parameters does not ameliorate the problem and thus further suggests possible subtle inconsistencies in the functional form; interestingly, the hydrogen-hydrogen RDF is immune from steepness of the leading edge. This may be due to the lack of LJ between hydrogens, although this would then also hold for the oxygen-hydrogen RDF, which in this case also suffers from the deficiency in the force field. Further studies are warranted.

1. Temperature dependence of radial distribution functions

To evaluate changes in structural features with temperature, the RDFs at elevated temperatures are shown in Fig. 4. The oxygen-oxygen RDFs (Fig. 4, left panel) clearly indicate the loss of structure with increasing temperature. By $T=400$ K, the second maximum essentially disappears and the third maximum is greatly diminished. The first peak experiences a general broadening and reduction in magnitude with increased temperature, corresponding to the breaking of hydrogen bonds. We also observe a shift in the primary peak position with increasing temperature, consistent with the previous simulations.[57] In this context it is appropriate to discuss the variation in the LJ parameters with temperature for the TIP4P-QDP-LJ model. At enhanced temperatures, the atomic charges (on average) will approach those of the gas phase and will result in an increased intermolecular attraction. Indeed there is an inherent tendency for the oxygen-oxygen distance to increase as the system becomes less dense (as demonstrated in Ref. 57); the effect of the charge dependent LJ parameters acts to oppose this shift in the oxygen-oxygen peak at higher temperatures. That is, this temperature dependence of the LJ parameters regulates the rate at which this peak shifts, which is also manifested in the shift in the coexistence curve (from that of TIP4P-QDP) toward higher condensed phase densities at higher temperatures.

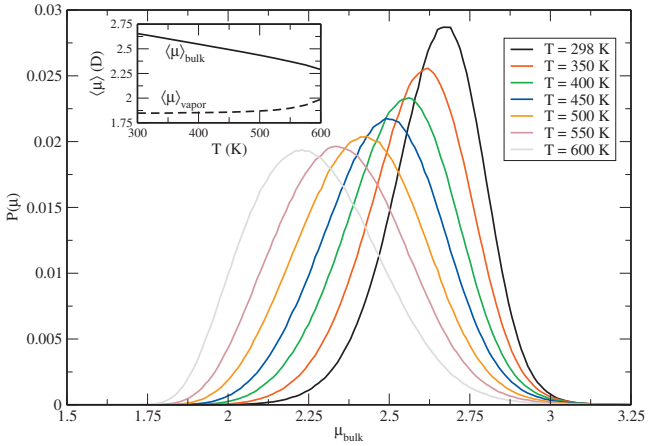

FIG. 5. Dipole moment distributions for TIP4P-QDP-LJ computed from bulk simulations at various temperatures. The inset features the temperature dependence of the average dipole moment in the bulk (solid line) and in the vapor (dashed line).

The diminished magnitude of the first peak in the O–H RDF (center panel) further supports the disruption of the hydrogen bonding. The height of the first maximum at $T=600$ K reduces to approximately half the value at $T=298$ K. Additionally, the separation between the first and second peaks of the O–H RDF becomes less distinct with increasing temperature; that is, the first minimum becomes less deep. This observation is consistent with *ab initio* MD results from Hura *et al.*[58] Interestingly, the second peak (solvation shell) is relatively unperturbed by changes in temperature. This suggests that the majority of structure loss occurs within the first solvation shell as increased thermal fluctuations allow interacting molecules to overcome energetically favorable hydrogen bonds. Hydrogen bond dependence on temperature is further explored in Sec. III E. Finally, we remark that the H–H RDFs demonstrate a general "washing out" of structure consistent with the O–O and O–H RDFs.

C. Dipole moment distributions

Dipole moment distributions (Fig. 5) are presented for various temperatures. A general broadening of the distribution and the shifting of the position of the maximum toward a lower average dipole moment are observed with increasing temperature. The inset of Fig. 5 demonstrates the variation in

the average bulk and average vapor dipole moment with temperature. In the vapor, the average dipole moment does not deviate significantly from the vacuum value until the temperature exceeds 500 K. Below this temperature, the concentration of water is low and interactions between vapor molecules are essentially negligible. Conversely, higher concentrations of water vapor above $T=500$ K result in more intermolecular interactions and the induction of higher dipole moments. The average condensed-phase dipole moment decreases essentially linearly until $\sim T=550$ K, after which point the decrease becomes more rapid; this is attributed to the increased rate at which the condensed-phase density decreases at temperatures approaching the critical point.

D. Enthalpy of vaporization

The enthalpy of vaporization is calculated as

$$\Delta H_{\mathrm{vap}} = \langle E_{\mathrm{gas}} \rangle - \langle E_{\mathrm{liq}} \rangle + RT, \tag{16}$$

where E_{liq} is the energy of a molecule in the condensed phase and E_{gas} is the energy of a molecule in the gas phase. As an initial approximation, we can estimate the latter quantity as the energy of a molecule in vacuum. This approximation is appropriate for low temperature (<450 K) vapor phases where the concentration is low enough to prevent significant interactions. However, as has been previously discussed, vapor-phase density becomes nontrivial at higher temperatures and this approximation no longer holds. Therefore, constant *NVT* simulations at the equilibrium vapor phase density as determined from interfacial simulations were conducted for systems at temperatures at 400 K or greater. For comparison, the temperature profiles of enthalpy of vaporization calculated using both the ideal gas approximation and the simulation E_{gas} are presented in Fig. 6. ΔH_{vap} at 298 K for TIP4P-QDP-LJ (10.47 ± 0.10 kcal/mol) demonstrates an excellent agreement with experiment and other state-of-the-art water models. This is expected since this was one of the target properties during the parametrization process. The excellent agreement of this property and experiment at multiple state points demonstrates the ability of TIP4P-QDP-LJ to capture relative energetics between phases. As anticipated in the above discussion, the values calculated for TIP4P-QDP-LJ using an ideal gas assumption show excellent agreement with experiment over the range $298\ \mathrm{K} < T < 500$ K, deviating more at elevated temperatures. Values calculated using the additional simulation of the vapor phase demonstrably improve accuracy at higher temperatures. Furthermore, the values calculated using this latter approach ultimately converge with those using the ideal gas approximation at lower temperatures. For simulations conducted at the experimental densities, the enthalpy of vaporization (shown in Fig. 6 as calculated using E_{gas} from *NVT* simulations at the experimental gas phase density) demonstrates better agreement with experiment than those at the simulation density, suggesting the relative energetics between the liquid and vapor phase is adequately represented at the correct densities. We finally note that the present approach to vaporization enthalpies does not include higher-order corrections such as discussed by Horn *et al.*[59] in parametrizing the TIP4P/Ewald

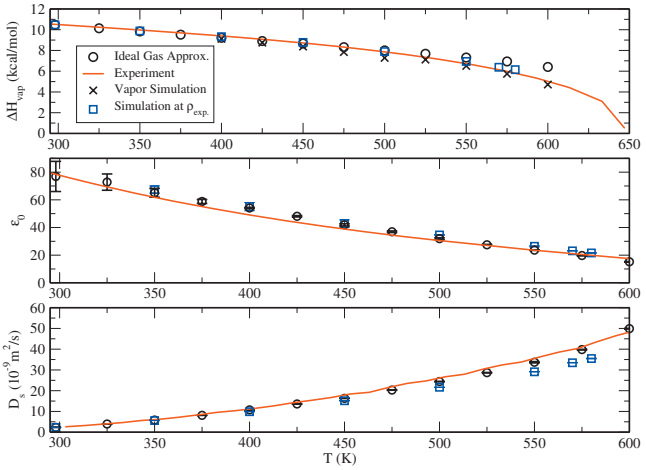

FIG. 6. TIP4P-QDP-LJ condensed phase properties from simulations at the model's coexistence densities (black circles), the experimental coexistence densities (blue squares), and experiment (solid red line). The upper panel demonstrates the dependence of the enthalpy of vaporization on temperature. Circles represent ΔH_{vap} values using the approximation that E_{gas} is the energy of an isolated TIP4P-QDP-LJ molecule, whereas X treat E_{gas} as the average energy of a TIP4P-QDP-LJ molecule in a gas-phase simulation at each temperature at the coexistence ρ_{vap}. Experimental enthalpies of vaporization are taken from Ref. 90. The center panel demonstrates the trend of decreasing dielectric constant with temperature for TIP4P-QDP-LJ and experiment (Ref. 90). The bottom panel demonstrates the increase in self-diffusion constant with increasing temperature for TIP4P-QDP-LJ and experiment (Ref. 100). Diffusion constants for TIP4P-QDP-LJ are corrected for infinite system size (Refs. 8 and 62).

model. Thus, within the formalism we have adopted, the vaporization enthalpies match well the available experimental data; inclusion of further corrections may deteriorate or not affect the accuracy demonstrated in the current study.

E. Hydrogen-bond profiles

We examine the average number of hydrogen bonds in the condensed and vapor phases as a function of temperature. For this analysis, we employ a geometric definition of a hydrogen bond in which the oxygen-oxygen distance is less than 3.5 Å and the O–O–H angle is less than 30°.[8,60,61] Additionally, the probability of hydrogen bond formation (inset of Fig. 7) is determined by the ratio of the number of hydrogen bonds formed by a molecule and its coordination number. The coordination number is taken as the number of molecules satisfying the distance criteria. Expectedly, the average number of hydrogen bonds in the condensed phase decreases steadily with increasing temperature. Although there is essentially no hydrogen bond formation in the vapor phase below $T=500$ K, the increased density of this phase at higher temperatures leads to greater opportunity for molecular interaction and the formation of some hydrogen bonds. This effect becomes increasingly drastic approaching the critical temperature, where the vapor density is maximized. Despite the rapid changes in the average hydrogen bonds at high temperatures, the fraction of hydrogen bond formation decreases approximately linear at higher temperatures. This can be rationalized in that although the average number of hydrogen bonds changes more rapidly at higher temperatures, there is also a corresponding change in the coordination number due to the increased rate of change in the den-

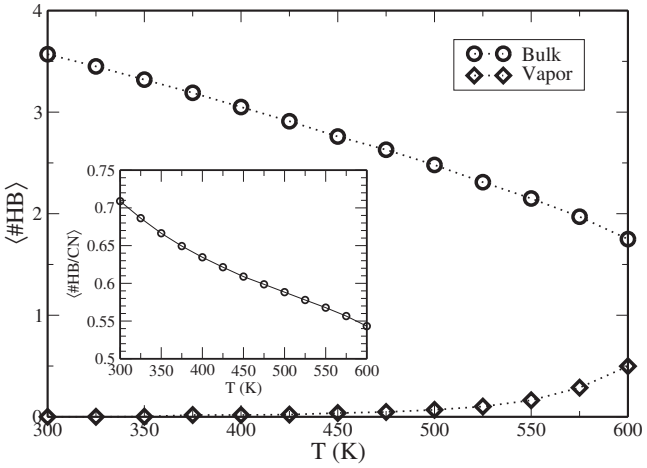

FIG. 7. Hydrogen bond temperature profiles for TIP4P-QDP-LJ for the bulk (circles) and vapor (diamonds) phases. Hydrogen bonds are defined using the geometric criteria of $R_{OO}<3.5$ Å and $\angle_{OOH}<30°$. The inset plot features the average fraction of hydrogen bonds relative to the coordinate number, which is defined using only the distance criteria of hydrogen bonding.

sity in each phase. The fraction of hydrogen bonds decreases most rapidly at the lower temperatures $T<450$ K, where the changes in density are relatively minor but the enhanced thermal energy allows for the breaking of hydrogen bonds. We note that this temperature range also exhibited significant loss of structural features in the RDFs.

F. Self-diffusion constant

The self-diffusion constant is calculated using the Einstein relationship

$$D_s = \lim_{t\to\infty} \frac{1}{6t} \langle (r(t) - r(0))^2 \rangle. \tag{17}$$

It has been previously suggested that the self-diffusion constant is inherently sensitive to the system size.[62] We have previously estimated a 1.1 multiplicative factor[8] as an appropriate correction for a system of 216 water molecules to an infinitely large one. All self-diffusion constants presented for TIP4P-QDP-LJ, including those in Fig. 6, have been corrected using this correction for system size. The self-diffusion constant for the TIP4P-QDP-LJ at 298 K, $2.30(\pm 0.01)\times 10^{-9}$ m^2/s, demonstrates an excellent agreement with the experiment (2.30×10^{-9} m^2/s) (Ref. 63) and the TIP4P-QDP value of $2.48(\pm 0.04)\times 10^{-9}$ m^2/s. At higher temperatures, the self-diffusion constant increases due to increased thermal energy leading to the breaking of hydrogen bonds and the loss of structure. We observe remarkably a strong agreement between the values calculated for TIP4P-QDP-LJ and experiment at elevated temperatures. The quality of the current model is equivalent to the GCPM model of Paricaud *et al.*[20] although the authors of that work performed *NVT* MD studies at the experimental densities. Additional simulations of TIP4P-QDP-LJ performed at the experimental coexistence density underpredict the experimental diffusion constants, resulting in generally poorer agreement than is seen considering the simulations at the model's coexistence density. Such an underprediction is anticipated on the basis on the effect of densification on reducing diffusion. We further remark that Paricaud *et al.*[20] only present the self-diffusion constants up to 350 K and begin to see an underprediction of the quantity. Our model performs similarly at the experimental densities in this temperature range.

G. Dielectric constant

For the bulk TIP4P-QDP-LJ systems at the temperature studied, the dielectric constants are computed using the relation

$$\epsilon = \epsilon_\infty + \frac{4\pi}{3k_B T\langle V\rangle}(\langle M^2\rangle - \langle \mathbf{M}\rangle \cdot \langle \mathbf{M}\rangle), \tag{18}$$

where $\mathbf{M}$ is the dipole moment of the simulation cell. The term ϵ_∞ is the dielectric constant at infinite frequency or optical dielectric constant. We estimate the magnitude of this term via the Clausius–Mossotti equation

$$\frac{\epsilon_\infty - 1}{\epsilon_\infty + 2} = \frac{4\pi\alpha(T)}{3\langle V(T)\rangle}, \tag{19}$$

where $\langle V(T)\rangle$ is the average molecular volume at temperature T and $\langle \alpha(T)\rangle$ is the average molecular polarizability at temperature T. Thus, we use the average molecular polarizability calculated using Eq. (5) to determine ϵ_∞. Although alternate methods for calculating the optical dielectric constant have previously been employed, such approaches tend to overestimate this value.[8] Furthermore, the total magnitude of this term is well below the uncertainty in the total dielectric constant and small inaccuracies in this term will be inconsequential in establishing trends with increasing temperature. We compute ϵ_∞ of TIP4P-QDP-LJ to be 1.69 at 298 K, which is reduced from the experimental value of 1.79,[64] similar to the TIP4P-FQ value (1.592) reported by Rick *et al.*[4] At the elevated temperatures studied (325–600 K) we observe a decrease in ϵ_∞ which becomes more drastic at higher temperatures [e.g., 1.64 (400 K), 1.55 (500 K), 1.40 (600 K)]. Although increasing polarizability works to increase the magnitude of ϵ_∞ while the increasing molecular volume with temperature decreases the magnitude of this property, the rate of change in the density with temperature is greater than that of polarizability for this model resulting in the net decrease in ϵ_∞ with increasing temperature.

The dielectric constant for TIP4P-QDP-LJ at 298 K was calculated to be 77 ± 11, which is in excellent agreement with the experiment and an improvement over the TIP4P-QDP value. In general, however, the dielectric constant for TIP4P-QDP-LJ is slightly higher than the experiment over the temperatures sampled. Furthermore, results at both the simulation at experimental densities are essentially equivalent in terms of their reproduction of experiment. The observed temperature dependence of the dielectric constant for the current model is commensurate to that of the GCPM of Paricaud *et al.*[20] It appears that a proper accounting of the state-dependent (or environment dependent) polarization effects (whether explicitly via polarizable electrostatics or in combination with the effects of dispersion) is important and that the similarities in the observed predictions of the present model and the GCPM model suggest the fundamental origins of these effects.

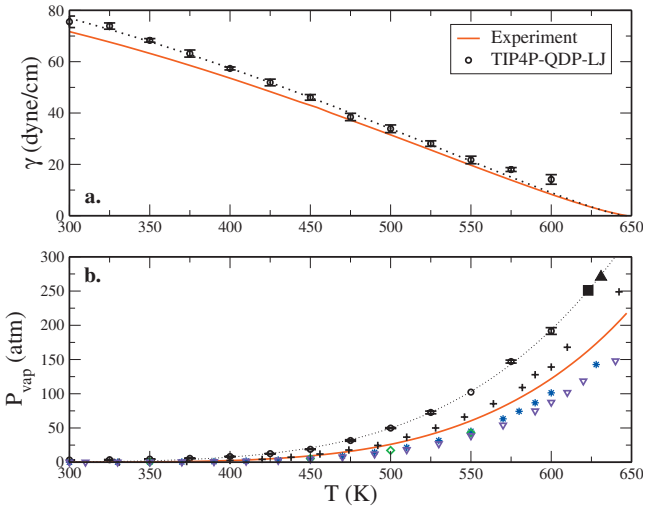

FIG. 8. (a) Surface tension and (b) vapor pressure profiles with temperature. Experimental surface tension data are taken from Ref. 101. The dotted line in panel (a) is the fit of Eq. (21) to the surface tension data from $T=300-550$ K (as discussed in the text), while the dotted line in the vapor pressure profile [panel (b)] represents the functional fit using Antoine's law. The additional symbols in panel (b) represent the vapor pressures of other water models (consistent with those in Fig. 2). The solid black square represents the critical pressure corresponding to the uncorrected critical temperature for TIP4P-QDP-LJ, while the solid black triangle corresponds to the critical pressure calculated using the corrected critical temperature. Experimental vapor pressure data are taken from Ref. 90.

H. Surface tension

The surface tension of liquid arises from the imbalance of intermolecular forces at the surface of a liquid-vapor interface. Due to the strength of its hydrogen bonds, water has a relatively high surface tension of 71.9 dyn/cm at 298 K.[65] However, as the temperature of the system increases, the cohesive forces at the surface diminish, resulting in a diminished energetic penalty for water molecules to leave the bulk for the interface; the free energy penalty for creating more surface (at constant volume) decreases. Thus, the surface tension of water will decrease with increasing temperature until a uniform fluid phase is reached (i.e., the critical point). In this regard, we calculate the surface tension for the liquid-vapor interface at each temperature considered from the difference in the normal and tangential elements of the internal pressure tensor[66]

$$\gamma = \frac{L_z}{2}\left(P_{zz} - \frac{P_{xx}+P_{yy}}{2}\right), \tag{20}$$

where P_{xx}, P_{yy}, and P_{zz} are the diagonal elements of the internal pressure tensor and L_z is the length of the simulation cell in the direction normal to the surface. The dependence of surface tension on temperature is presented in Fig. 8(a). Although this quantity is consistently higher than the experimental values, the qualitative trend is matched. That the current model systematically overestimates surface tension at lower temperatures may be due to an insufficient/incorrect form of the polarizability and repulsion/dispersion interaction scaling function or to a need for further refinement and/or fine tuning of the water-water interaction modulation in the interfacial region. Moreover, as the surface tension is derived from the difference in the normal and tangential pressure tensor components, an overestimation of the surface tension suggests that the normal component is not described well by the model; this is self-consistently borne out by the overestimation of the vapor pressure (as determined as the normal component of the pressure tensor from *NVT* simulations), as shown in Fig. 8(b).

We next consider the prediction of the critical temperature (T_c) from the computed surface tension data. Following the approach of Vega and de Miguel,[67] we correlate our surface tension data to the expression

$$\gamma(T) = a\left(1-\frac{T}{T_c}\right)^{\mu}\left(1+b\left(1-\frac{T}{T_c}\right)\right), \tag{21}$$

where a, b, and T_c are treated as fitting parameters. The exponent μ is set to 11/9 as first suggested by Guggenheim[68] and recently applied by Vega and de Miguel.[67] In order to compare to the results of Vega and de Miguel[67] we only include data up to $T=550$ K (as done by Vega and de Miguel[67]) for the current fitting. Issues related to the surface tension calculation at elevated temperatures nearing the critical temperature are discussed below. From the surface tension data, we estimate a critical temperature for TIP4P-QDP-LJ, $T_c=645\pm7$ K. Although this value overestimates the critical temperature as estimated from the Wegner expansion fit of the coexistence envelope ($T_c=623$ K), it is in good agreement with the prediction from extrapolation of the interfacial thickness ($T_c=640$ K). Moreover, the surface tension based critical temperature is overestimated much as observed for other fixed-charge water models shown recently.[67] Furthermore, based on our analysis of the prediction of critical temperature based on a Wegner fit to the experimental liquid-vapor envelope, we also realize that the critical temperature predicted by fitting the liquid-vapor envelope is lower than that predicted by surface tension data analysis.

We return to the nature of the curvature of the surface tension curve in Fig. 8(a). The current model shows the weakly sigmoidal functional form observed for nonpolarizable, fixed-charge water models as shown by Vega and de Miguel.[67] At higher temperatures, the curvature begins to change approaching the critical point, a behavior ascribed in general to strongly associating fluids.[67] In the current work, we observe that beginning at 550 K, the curvature of the surface tension data displays a significant shift in curvature. This is in contrast to previously reported results with nonpolarizable water models (although we note that in Ref. 67, some water models show a systematic drift to higher values of surface tension than obtained from the correlation curve as one approaches the critical temperature).

We posit that at elevated temperatures (575, 600 K) studied in this work, the nature of the bulk phases is not as rigorously defined, the implication being the following: the nature of the vapor-liquid interface is no longer fundamentally planar (significant fluctuations of the Gibbs dividing surface on the order of 10 Å at 600 and 575 K compared to less than 1 Å at 298–350 K and 2 and 3 Å from 350–450 K) and the surface tension definition is no longer rigorously applicable in the form of Eq. (20). Further observations of the interfacial systems at 575 and 600 K (via analysis of MD snapshots and animations of simulation trajectories) demon-

strate rather large deformations of the interface, suggesting that the current system formulation of the interface may not allow an accurate sampling of normal and tension forces comprising the macroscopic surface tension at these elevated temperatures. In light of such system behavior, we adopt the approach of limiting the range of surface tension data to use for estimating the critical temperature based on surface tension data to values up to 550 K as done in previous studies. We reiterate that the current surface tension data with the caveats just discussed are self-consistent with the predictions of critical parameters based on fits to the coexistence liquid-vapor densities of Fig. 1. We note that the use of the *bulk* liquid and vapor densities obtained at the elevated temperatures nearing the critical temperature is still valid as equilibrium bulk phases of sufficiently large spatial extent are generated and persist for the duration of the simulation. Alternative approaches to the binodal, such as the Gibbs–Duhem integration method,[89] would prove insightful and are being pursued in our laboratory.

I. Vapor pressure

The vapor pressure is taken as $P_{\mathrm{vap}}=P_{zz}=P_{\mathrm{normal}}$.[69,70] The vapor pressures calculated for each temperature are presented in Fig. 8(b). P_{vap} for TIP4P-QDP-LJ is consistently higher than the experiment, deviating most at higher temperatures. From the vapor pressure data, we can estimate the critical pressure P_c using Antoine's law[7,71]

$$\ln(P) = A + \frac{B}{T+C}, \tag{22}$$

where A, B, C are adjustable parameters used in the fit determined to be $A=13.44$, $B=-5733$, $C=101.7$. P_c was then obtained by solving for pressure at the critical temperature of the model. We compute $P_c=250.9$ atm for the uncorrected critical data and $P_c=270.6$ atm for the corrected data. Although these pressures overestimate the experimental value of 218 atm by about 30–50 atm (15%–24%), this agreement is relatively acceptable considering critical pressures calculated using state-of-the-art nonpolarizable models can underestimate the experiment by almost 60%.

We note that the vapor pressure and vaporization enthalpy (both computed in this study) are thermodynamically related via the Clapeyron equation. It may be surprising that the vaporization enthalpy computed using Eq. (16) is in much better agreement with the experiment compared to the vapor pressures given the connection of the two via the Clapeyron expression. However, we emphasize that the two properties are independently determined from a simulation, and due to the empirical force field used to generate the thermodynamic ensembles at the various state points, any departure of the predicted properties from experiment is due to error in the force field. Thus, it is not surprising that vapor pressures predicted using computed vaporization enthalpies and the Clapeyron equation differ from values calculated from the system virial (the latter depending on the forces and intermolecular potential). We acknowledge this weakness of the current force field. Furthermore, the Clapeyron equation includes the volume change in vaporization along the VLE line. Since in the present simulations the densities along the VLE envelope are not predicted to 100% accuracy, the deviation of the predicted trends in vapor pressure and vaporization enthalpies from the predictions of the Clapeyron equation are embodied in the volume change term; moreover, to reiterate, this behavior is thus self-consistent.

Finally, we show in Fig. 8(b) the results of vapor pressure prediction from other water models including GCPM, SPC/E, TIP4P-FQ, and TIP4P-2005. We observe that most water models perform similarly up to roughly 450 K when the TIP4P-QDP-LJ model begins to deviate first. The TIP4P-FQ and TIP4P-2005 both underestimate experimental vapor pressure and thus perform quite similarly.

J. Interfacial potential

As a final measure of the combined electrostatic and orientational changes with temperature, we consider the interfacial potential over the range of temperatures studied. We consider the interfacial potential as the difference between the gas-phase Volta outer potential and the liquid phase Galvani inner potentials as defined in standard treatments[72–76] and considered in rather elegant detail recently.[76–79] The Volta outer potential is the work to bring a unit point charge (no excluded volume) from infinity to the vapor side of the liquid-vapor interface; the Galvani inner potential is the work to transfer a unit point charge from the vapor through the interface and into the bulk liquid.[76] In keeping with previous studies,[80–83] we calculate this property by doubly integrating the z-component (surface normal) of the charge density as follows:

$$\Delta\Phi(z) = \Phi(z) - \Phi(z_0) = \int_{z_0}^{z} dz' \int_{z_0}^{z'} dz'' \rho(z), \tag{23}$$

where z_0 specifies the center of mass of the bulk slab. This potential can be decomposed into contributions arising from the total water dipole contribution ($\Delta\Phi_M$) and the water quadrupole contribution ($\Delta\Phi_Q$).[19] The dipole moment contribution is computed via integration of the water dipole moment density $P_z(z)$ over z according to[19,84,85]

$$\Delta\Phi_M = -\frac{1}{\epsilon_0}\int_{z_0}^{\infty} dz P_z(z), \tag{24}$$

where the dipole moment density is defined as

$$P_z(z) = \left\langle \sum_m \delta(z - z_m)\left(\sum_i q_{im} z_{im}\right)\right\rangle. \tag{25}$$

The quadrupole contribution is calculated from the local molecular quadrupole density $Q_{zz}(z)$ and a reference value Q_{zz}°,

$$\Delta\Phi_Q(z) = -\frac{1}{\epsilon_0}|Q_{zz}(z) - Q_{zz}^{\circ}|. \tag{26}$$

We take the reference $Q_{zz}^{\circ}=0$ and define the quadrupole moment density[84,85] as

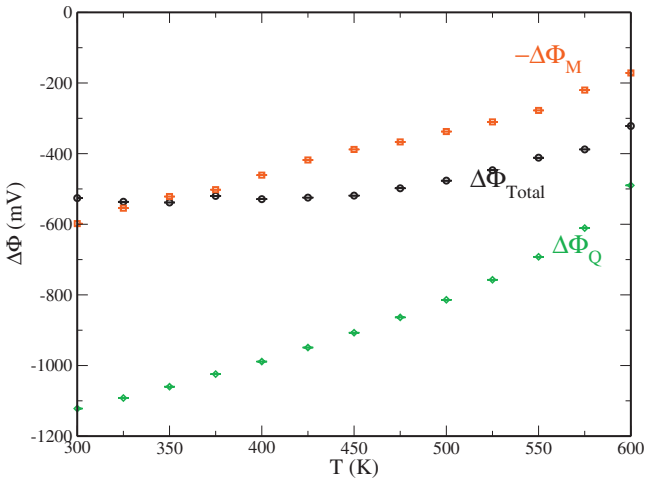

FIG. 9. Interfacial potential and its decomposition into dipole ($\Delta\Phi_M$) and quadrupole contributions ($\Delta\Phi_Q$). The dipole contribution is presented as $-\Delta\Phi_M$ to allow for direct comparison of the relative changes in the quadrupole contribution.

$$Q_{zz}(z) = \left\langle \sum_m \delta(z - z_m)\left(\frac{1}{2}\sum_i q_{im} z_{im}^2\right)\right\rangle. \quad (27)$$

Figure 9 shows the change in interfacial potential and its components with temperature. We note that the presented total interfacial potentials ($\Delta\Phi_{tot}$) were calculated using Eq. (23) and they deviate from the sum of the dipole and quadrupole contributions by ~4 mV. This difference is within the statistical uncertainty associated with each potential indicating the self-consistency in the two methods of calculation. For temperatures less than 450 K, the interfacial potential fluctuates between values of 520–540 mV, which is consistent with the values calculated using TIP4P-FQ and TIP4P-QDP at 298 K,[8] as well as numerous other water force fields. As seen in the decomposition, $\Delta\Phi_M$ and $\Delta\Phi_Q$ decrease in magnitude at slightly different rates, resulting in a negative slope $d\Phi/dT$ for temperatures up roughly 350 K; the slope obtained for the current model is (−0.25 mV/K). We obtain this value from the slope of a least-squares linear fit to the interfacial potentials calculated for $T=300-350$ K. The sign agrees well with the experiment (−0.27 mV/K) as well as the values of Sokhan and Tildesley[19] (using SPC/E), −1 mV/K, and Dang and co-workers[86,87] (using their polarizable model), −1.2 mV/K (all at 298 K). The rate of change in the dipole moment contribution is greatest at the lower temperatures. Since the dipole contribution is intimately connected to changes in the orientational structure of water, the high rate of change in dipole contribution is expected due to the previously noted rapid rate of structural change at these temperatures. Conversely, the quadrupole contribution, which has a dependence on the density difference between the two phases, decays most rapidly at higher temperatures as the densities of the condensed and vapor phases converge and the variation in density difference is greatest.[19] In agreement with the simulations of Sokhan and Tildesley,[19] both the contributions monotonically approach zero as the temperature approaches the critical point. Such changes would result in zero interfacial potential at the critical point, which is expected for uniform phase. Interestingly, much as Sokhan and Tildesley,[19] we observe a slight minimum in the total surface potential at 350 K. Whether this is purely coincidental or a manifestation of a more fundamental underlying effect is beyond the scope of this study (but presents an interesting question for further work). We finally note that the nature of the total surface potential of the water liquid-vapor interface is generally predicted to be negative using most polarizable and nonpolarizable force fields. Also, recent *ab initio* MD study by Kathmann *et al.*[76] demonstrated that the water surface potential is −18 mV, at least qualitatively bearing out the sign predicted by classical force fields.

IV. DISCUSSION AND CONCLUSIONS

We have presented a modified version of the TIP4P-QDP water model previously developed in our laboratory. The water model TIP4P-QDP-LJ accounts for the change in the dispersion and repulsion interactions between water molecules as a function of the polarizability of the molecule. Within the formalism of the TIP4P-QDP water model, this maps onto the variation in the LJ interactions with molecular dipole moment, and more fundamentally, atomic charge (in this case, the charge on the virtual *M*-site of the TIP4P model). The motivation for such an undertaking is to fully develop the concept of modeling phase dependent polarizability as introduced in the TIP4P-QDP model. Fully accounting for phase dependent polarizability had profound benefits for reproducing the liquid-vapor coexistence curve compared to analogous models in which no treatment of phase-dependent polarizability was considered (TIP4P-FQ) and in which only the molecular hardnesses varied with phase (TIP4P-QDP). The level of agreement with experimental properties at various temperatures (self-diffusion constants, enthalpy of vaporization, dielectric constants, etc.) is remarkable considering this model was only fit to gas-phase properties and bulk properties at 298 K. Furthermore, we find that the temperature coefficient of the surface potential (rate of change in surface potential with temperature) is in qualitative agreement with previous molecular simulation studies as well as experiment. However, despite the successes of the model, it also has shortcomings. First, we mention that the dependence of the LJ terms on the average charge between two water molecules inherently necessitates additional parametrization for use with other chemical entities. Furthermore, TIP4P-QDP-LJ has not been successful in the reproduction of the temperature at maximum density (data not shown). Much like the TIP3P water model, there appears to be broad transition between liquid and solid at temperatures below ambient conditions. This may be related to the omission of a linear term in the charge dependence of the dispersion/repulsion nonbonded terms. Ongoing work will determine the sensitivity of the model to this parameter. We note that in the final analysis, a systematic addition of further physical effects into the TIP4P-QDP water systematically resulted in an improvement of the coexistence properties. We believe that further tuning of the model is warranted and will provide a more accurate (if not quantitative) water model applicable over a broad range of thermodynamic state points.

Admittedly, the complexity of our water model appears

superficially exorbitant; however, upon closer examination, it is no more computationally expensive compared to the original TIP4P-FQ and TIP4P-QDP water models. As reported in a previous study, the TIP4P-FQ and TIP4P-QDP water models require effectively equivalent overhead with regard to fixed charge force fields using standard LJ and particle mesh Ewald schemes. For the TIP4P-QDP-LJ model, the varying LJ parameters are facilely absorbed into the calculation of the usual pair interactions, and thus introduce no extra cost. When running identical calculations with each of the QDP models, we observed that TIP4P-QDP requires 1.002 times the computational cost of TIP4P-FQ; TIP4P-QDP-LJ performs at 1.025 times the computational cost of TIP4P-FQ.

Future studies will probe the effects of varying the contributions of the repulsive and dispersion components of the charge-dependent LJ interaction on the predictions of vapor-liquid equilibria. We acknowledge that this, to some extent, moves away from the philosophy of parametrizing physical models to only one state point with the goal of realizing broad transferability. Nevertheless, an independent study on the potential capability of such models on an equal footing (with respect to parametrization based on data over a range of thermodynamic state points as has been traditionally done[9]) would provide further insight into the fundamental mechanisms associated with such interfaces. Moreover, from a biological perspective, studies of the nature of lipid-water interactions would also prove stimulating. It has been shown that the dipole moment of water molecules in the center of a lipid bilayer[88] is dramatically lower than that in the bulk, reaching values equivalent to that in the gas phase. This physical behavior coupled with the variation in polarizability and molecular size as in the TIP4P-QDP-LJ, we expect, will result in nontrivial differences in lipid-water interaction energetics, dynamics, and structure. Studies along those lines continue in our laboratory.

ACKNOWLEDGMENTS

The authors gratefully acknowledge the financial support from an NIH COBRE (Center of Biomedical Research Excellence) at the University of Delaware, Department of Chemistry and Biochemistry (Molecular Design of Advanced Biomaterials: Grant No. 2P20RR017716-06A1). The authors also wish to thank Professor Alan K. Soper for providing the most recent experimental radial distribution function data shown in Fig. 3.

[1] W. L. Jorgensen and J. Tirando-Rives, Proc. Natl. Acad. Sci. U.S.A. **102**, 6665 (2005).
[2] B. Guillot, J. Mol. Liq. **101**, 219 (2002).
[3] C. Vega, J. L. F. Abascal, M. M. Conde, and J. L. Aragones, Faraday Discuss. **141**, 251 (2009).
[4] S. W. Rick, S. J. Stuart, and B. J. Berne, J. Chem. Phys. **101**, 6141 (1994).
[5] G. Lamoureux, A. D. MacKerell, Jr., and B. Roux, J. Chem. Phys. **119**, 5185 (2003).
[6] W. L. Jorgensen, J. Chandrasekhar, J. D. Madura, R. W. Impey, and M. L. Klein, J. Chem. Phys. **79**, 926 (1983).
[7] C. Vega and J. L. F. Abascal, J. Chem. Phys. **125**, 034503 (2006).
[8] B. A. Bauer, G. L. Warren, and S. Patel, J. Chem. Theory Comput. **5**, 359 (2009).
[9] B. Chen, J. Xing, and J. I. Siepmann, J. Phys. Chem. B **104**, 2391 (2000).
[10] A. A. Chialvo, A. Bartok, and A. Baranyai, J. Mol. Liq. **129**, 120 (2006).
[11] A. Baranyai, A. Bartok, and A. A. Chialvo, J. Mol. Liq. **134**, 94 (2007).
[12] M. G. Martin and J. I. Siepmann, J. Phys. Chem. B **102**, 2569 (1998).
[13] B. Chen, J. J. Potoff, and J. I. Siepmann, J. Phys. Chem. B **105**, 3093 (2001).
[14] C. D. Wick, J. M. Stubbs, N. Rai, and J. I. Siepmann, J. Phys. Chem. B **109**, 18974 (2005).
[15] N. Lubna, G. Kamath, J. J. Potoff, N. Rai, and J. I. Siepmann, J. Phys. Chem. B **109**, 24100 (2005).
[16] J. J. Potoff and J. I. Siepmann, AIChE J. **47**, 1676 (2001).
[17] J. M. Stubbs, J. J. Potoff, and J. I. Siepmann, J. Phys. Chem. B **108**, 17596 (2004).
[18] N. Yoshii, R. Miyauchi, S. Miura, and S. Okazaki, Chem. Phys. Lett. **317**, 414 (2000).
[19] V. P. Sokhan and D. J. Tildesley, Mol. Phys. **92**, 625 (1997).
[20] P. Paricaud, M. Predota, A. A. Chialvo, and P. T. Cummings, J. Chem. Phys. **122**, 244511 (2005).
[21] W. F. Murphy, J. Chem. Phys. **67**, 5877 (1977).
[22] A. Krishtal, P. Senet, M. Yang, and C. van Alsenoy, J. Chem. Phys. **125**, 034312 (2006).
[23] B. Schropp and P. Tavan, J. Phys. Chem. B **112**, 6233 (2008).
[24] A. Morita, J. Comput. Chem. **23**, 1466 (2002).
[25] R. T. Sanderson, *Chemical Bonds and Bond Energy* (Academic, New York, 1976).
[26] S. Patel and C. L. Brooks III, Mol. Simul. **32**, 231 (2006).
[27] S. W. Rick and B. J. Berne, J. Am. Chem. Soc. **118**, 672 (1996).
[28] S. Patel, A. D. MacKerell, and C. L. Brooks III, J. Comput. Chem. **25**, 1504 (2004).
[29] A. K. Rappe and W. A. Goddard III, J. Phys. Chem. **95**, 3358 (1991).
[30] R. T. Sanderson, Science **114**, 670 (1951).
[31] R. Chelli and P. Procacci, J. Chem. Phys. **117**, 9175 (2002).
[32] P. Itskowitz and M. L. Berkowitz, J. Chem. Phys. **101**, 5687 (1997).
[33] S. W. Rick, S. J. Stuart, J. S. Bader, and B. J. Berne, J. Mol. Liq. **65–66**, 31 (1995).
[34] S. W. Rick, J. Chem. Phys. **114**, 2276 (2001).
[35] S. W. Rick and S. J. Stewart, *Reviews of Computational Chemistry* (Wiley, New York, 2002).
[36] B. R. Brooks, R. E. Bruccoleri, B. D. Olafson, D. J. Stages, S. Swaminathan, and M. J. Karplus, J. Comput. Chem. **4**, 187 (1983).
[37] C. L. Brooks III, M. Karplus, and B. M. Pettitt, *A Theoretical Perspective of Dynamics, Structure, and Thermodynamics* (Wiley, New York, 1988), Vol. LXXI.
[38] J. I. Steinfeld, J. S. Francisco, and W. L. Hase, *Chemical Kinetics and Dynamics*, 2nd ed. (Prentice-Hall, Englewood Cliffs, NJ, 1999).
[39] T. Darden, D. York, and L. Pedersen, J. Chem. Phys. **98**, 10089 (1993).
[40] S. Nose, Mol. Phys. **52**, 255 (1984).
[41] J. S. Huang and W. W. Webb, J. Chem. Phys. **50**, 3677 (1969).
[42] D. Beysens and M. Robert, J. Chem. Phys. **87**, 3056 (1987).
[43] A. E. Ismail, G. S. Grest, and M. J. Stevens, J. Chem. Phys. **125**, 014702 (2006).
[44] I. W. Kuo, C. J. Mundy, B. L. Eggimann, M. J. McGrath, J. I. Siepmann, B. Chen, J. Vieceli, and D. J. Tobias, J. Phys. Chem. B **110**, 3738 (2006).
[45] J. Alejandre, D. J. Tildesley, and G. A. Chapela, J. Chem. Phys. **102**, 4574 (1995).
[46] G. A. Chapela, G. Saville, S. M. Thompson, and J. S. Rowlinson, J. Phys.: Condens. Matter **73**, 1133 (1977).
[47] E. M. Blokhuis, D. Bedeaux, C. D. Holcomb, and J. A. Zollweg, Mol. Phys. **85**, 665 (1995).
[48] B. Widom, J. Phys. Chem. **86**, 869 (1982).
[49] L. Vega, E. de Miguel, L. F. Rull, G. Jackson, and I. A. McLure, J. Chem. Phys. **96**, 2296 (1992).
[50] J. Alejandre, J. L. Rivera, M. A. Mora, and V. de la Garza, J. Phys. Chem. B **104**, 1332 (2000).
[51] S. Patel and C. L. Brooks III, J. Chem. Phys. **122**, 024508 (2005).
[52] *Perry's Chemical Engineers' Handbook*, edited by R. H. Perry and D. W. Greed (McGraw-Hill, New York, 1984).
[53] M. Mezei, Mol. Simul. **9**, 257 (1992).
[54] J. R. Errington and A. Z. Panagiotopoulos, J. Phys. Chem. B **102**, 7470 (1998).
[55] X. B. Zhang, Q. L. Liu, and A. M. Zhu, Fluid Phase Equilib. **262**, 210 (2007).
[56] A. K. Soper, J. Phys.: Condens. Matter **19**, 335206 (2007).
[57] A. K. Soper, Chem. Phys. **258**, 121 (2000).
[58] G. Hura, D. Russo, R. M. Glaeser, T. Head-Gordon, M. Krack, and M. Parrinello, Phys. Chem. Chem. Phys. **5**, 1981 (2003).

[59] H. W. Horn, W. C. Swope, J. W. Pitera, J. D. Madura, T. J. Dick, G. L. Hura, and T. Head-Gordon, J. Chem. Phys. **120**, 9665 (2004).
[60] P. Liu, E. Harder, and B. J. Berne, J. Phys. Chem. B **109**, 2949 (2005).
[61] F. Starr, J. Nielsen, and H. Stanley, Phys. Rev. **62**, 579 (2000).
[62] T. F. Miller III and D. E. Manolopoulos, J. Chem. Phys. **123**, 154504 (2005).
[63] K. Krynicki, C. D. Green, and D. W. Sawyer, Discuss. Faraday Soc. **66**, 199 (1978).
[64] A. D. Buckingham, Proc. R. Soc. London, Ser. A **238**, 235 (1956).
[65] R. Cini, G. Logio, and A. Ficalbi, J. Colloid Interface Sci. **41**, 287 (1972).
[66] J. G. Kirkwood and F. P. Buff, J. Chem. Phys. **17**, 338 (1949).
[67] C. Vega and E. de Miguel, J. Chem. Phys. **126**, 154707 (2007).
[68] E. A. Guggenheim, J. Chem. Phys. **13**, 253 (1945).
[69] A. R. Imre, G. Mayer, G. Hazi, R. Rozas, and T. Kraska, J. Chem. Phys. **128**, 114708 (2008).
[70] C. Ibergay, A. Ghoufi, F. Goujon, P. Ungerer, A. Boutin, B. Rousseau, and P. Malfreyt, Phys. Rev. E **75**, 051602 (2007).
[71] J. S. Rowlinson and F. L. Swinton, *Liquids and Liquid Mixtures* (Butterworths, London, 1982).
[72] W. R. Fawcett, *Liquids, Solutions, and Interfaces: From Macroscopic Descriptions to Modern Microscopic Details* (Oxford University Press, New York, 2004).
[73] J. Koryta, J. Dvorak, and L. Kavan, *Principles of Electrochemistry* (Wiley, New York, 1993).
[74] A. J. Bard and L. R. Faulkner, *Electrochemical Methods: Fundamentals and Applications* (Wiley, New York, 1980).
[75] A. W. Adamson, *Physical Chemistry of Surfaces* (Wiley, New York, 1990).
[76] S. M. Kathmann, I. W. Kuo, and C. J. Mundy, J. Am. Chem. Soc. **130**, 16556 (2008).
[77] D. Asthagiri, L. R. Pratt, and H. S. Ashbaugh, J. Chem. Phys. **119**, 2702 (2003).
[78] M. A. Kastenholz and P. H. Hünenberger, J. Chem. Phys. **124**, 124106 (2006).
[79] P. H. Hünenberger and J. A. McCammon, J. Chem. Phys. **110**, 1856 (1999).
[80] M. A. Wilson, A. Pohorille, and L. R. Pratt, J. Chem. Phys. **88**, 3281 (1988).
[81] L. X. Dang and T. M. Chang, J. Chem. Phys. **106**, 8149 (1997).
[82] S. Patel and C. L. Brooks III, J. Chem. Phys. **123**, 164502 (2005).
[83] L. X. Dang, J. Phys. Chem. B **105**, 804 (2001).
[84] M. A. Wilson, A. Pohorille, and L. R. Pratt, J. Chem. Phys. **90**, 5211 (1989).
[85] J. D. Jackson, *Classical Electrodynamics*, 3rd ed. (Wiley, New York, 1998).
[86] C. D. Wick, L. X. Dang, and P. Jungwirth, J. Chem. Phys. **125**, 024706 (2006).
[87] L. X. Dang and T.-M. Chang, J. Phys. Chem. B **106**, 235 (2002).
[88] J. E. Davis, O. Rahaman, and S. Patel, Biophys. J. **96**, 385 (2009).
[89] J. L. F. Abascal and C. Vega, J. Chem. Phys. **123**, 234505 (2005).
[90] *CRC Handbook of Chemistry and Physics*, 88th ed., edited by D. R. Lide (CRC, 6-4 to 16, 2008).
[91] K. Watanabe and M. L. Klein, Chem. Phys. **131**, 157 (1989).
[92] L. A. Curtiss, D. J. Frurip, and M. Blander, J. Chem. Phys. **71**, 2703 (1979).
[93] E. M. Mas, R. Bukowski, K. Szalewicz, G. C. Groenenboom, P. E. S. Wormer, and A. van der Avoird, J. Chem. Phys. **113**, 6687 (2000).
[94] A. Baranyai and A. Bartok, J. Chem. Phys. **126**, 184508 (2007).
[95] J. J. de Pablo and J. M. Prausnitz, J. Chem. Phys. **93**, 7355 (1990).
[96] Y. Guissani and B. Guillot, J. Chem. Phys. **98**, 8221 (1993).
[97] M. Lisal, W. R. Smith, and I. Nezbeda, Fluid Phase Equilib. **181**, 127 (2001).
[98] M. Lisal, J. Kolafa, and I. Nezbeda, J. Chem. Phys. **117**, 8892 (2002).
[99] E. W. Lemmon, M. O. McLinden, and M. L. Huber, NIST Standard Reference Database 23.
[100] K. Yoshida, N. Matubayasi, and M. Nakahara, J. Chem. Phys. **129**, 214501 (2008).
[101] N. B. Vargaftik, B. N. Volkov, and L. D. Voljak, J. Phys. Chem. Ref. Data **12**, 817 (1983).